Generation and Escape of Local Waves from the Boundary of Uncoupled Cardiac Tissue

Vadim N. Biktashev,* Ara Arutunyan,[†] and Narine A. Sarvazyan[†]

*Department of Mathematical Sciences, University of Liverpool, Liverpool L69 7ZL, United Kingdom; and [†]Pharmacology and Physiology Department, The George Washington University, Washington, District of Columbia

ABSTRACT   We aim to understand the formation of abnormal waves of activity from myocardial regions with diminished cell-to-cell coupling. En route to this goal, we studied the behavior of a heterogeneous myocyte network in which a sharp coupling gradient was placed under conditions of increasing network automaticity. Experiments were conducted in monolayers of neonatal rat cardiomyocytes using heptanol and isoproterenol as means of altering cell-to-cell coupling and automaticity, respectively. Experimental findings were explained and expanded using a modified Beeler-Reuter numerical model. The data suggest that the combination of a heterogeneous substrate, a gradient of coupling, and an increase in oscillatory activity of individual cells creates a rich set of behaviors associated with self-generated spiral waves and ectopic sources. Spiral waves feature a flattened shape and a pin-unpin drift type of tip motion. These intercellular waves are action-potential based and can be visualized with either voltage or calcium transient measurements. A source/load mismatch on the interface between the boundary and well-coupled layers can lock wavefronts emanating from both ectopic sources and rotating waves within the inner layers of the coupling gradient. A numerical approach allowed us to explore how 1), the spatial distribution of cells, 2), the amplitude and dispersion of cell automaticity, and 3), the speed at which the coupling gradient moves in space affect wave behavior, including its escape into well-coupled tissue.

INTRODUCTION

A bulk of evidence suggests that arrhythmogenic ectopic beats may originate from the areas of diminished cell-to-cell coupling (1). Such areas can be anatomical or functional. Anatomical examples of myocardial tissue with diminished coupling include an infarct scar (2,3), inflammatory infiltration (4), diffuse fibrofatty tissue responsible for arrhythmogenic right ventricular dysplasia syndrome (5), changes in myocardial fiber orientation (6), or an island of engrafted stem cells (7). Functional uncoupling occurs during ischemia as a result of the acidic environment and fatty acid accumulation, both of which diminish gap junctional conductance (1,8,9).

Between myocytes within areas of diminished cell-to-cell coupling and the surrounding well-coupled cell layers, there is a boundary layer with transitional values of coupling. This article considers possible behavior of tissue within such a boundary layer during conditions that promote cell automaticity. The latter can occur during ischemia or reperfusion as a result of catecholamine release or calcium overload, respectively. Indeed, it has been shown that ischemia leads to a 100-fold increase in concentration of interstitial catecholamines, which come from ischemic nerve endings (10). Thus, it is likely that during conditions of diminished blood flow the layers of poorly coupled cells can be awash in norepinephrine-containing interstitial fluid. The effects could be further exaggerated in areas that exhibit elevated adrenergic respon-siveness, an effect known as denervation supersensitivity (11). Reperfusion-associated automaticity, on the other hand, is attributed to calcium overload (12). Diffusion of neurotransmitters from neighboring regions contributes to the reperfusion-induced increase in intracellular calcium, giving rise to triggered activity (13).

The boundary layer is likely to comprise a small volume of tissue (a few millimeters wide, or a few hundred cells across) and be hidden under layers of normally oxygenated myocardium. Thus, on a whole-heart level, an abnormal wave emanating from such a region can appear as a single ectopic beat. To date, little is known of what lies beneath these macroscopic events. This is because the technical means to visualize the initial steps of ectopic beat generation in vivo, on a cellular level, are yet to be developed. Therefore, we attempted to gain initial insights into this process using in vitro networks of cardiac cells and to expand our experimental findings with numerical studies. Specifically, we asked: What is the behavior of a heterogeneous cardiac cell network when a gradient of cell-to-cell coupling is superimposed with an increase in cell automaticity? The experimental and modeling data suggested the existence of rich and interesting patterns, which included the formation of multiple automatic sources and spiral waves. Their behavior and ultimate fate were dependent on the movement of the boundary in space, degree of cell network heterogeneity, and other factors considered below.

METHODS

Cardiomyocyte culture

Cardiomyocytes from 2-day-old Sprague-Dawley rats were obtained using an enzymatic digestion procedure (14) in accordance with the guidelines of

the Institutional Animal Care and Use Committee. The cells were plated on 25-mm laminin-coated glass coverslips (10^5 cells/cm^2) and kept under standard culture conditions in Dulbecco-modified minimum essential medium supplemented with 5% FBS, 10 U/ml penicillin, 10 μg/ml gentamicin, and 1 μg/ml streptomycin. By day 3 in culture, the cells had formed interconnected confluent networks and were used in experiments for an additional 3–4 days.

Experimental chamber

A custom-made experimental chamber was used to perfuse a small area of a cell network with a solution of interest while events were observed under the microscope (Fig. 1 A). The design of the chamber and its flow characteristics have been previously described (14,15). It uses a stainless steel holder to mount a glass coverslip on the raised surface of a plastic holder, which contains two inlets and one outlet (Fig. 1). The polished sides of the chamber provide an airtight contact with the coverslip, whereas the Plexiglas ceiling creates a 300-μm perfusion space. Superfusion solutions are driven by a multisyringe pump from Harvard Apparatus (Holliston, MA) loaded with 10- and 30-ml glass syringes.

Experimental protocol

First an island of uncoupled cells was created by locally applying 2 mM heptanol (Fig. 1 B, area shown in solid gray). In the past, we have shown that 2 mM heptanol fully uncouples cells in our preparations (16,17). Washout was started by switching off inlet 2 and allowing 5 μM isoproterenol-containing Tyrode to gradually shrink the uncoupler-containing inner area. Because the

chamber has a closed design (Fig. 1 A, right), such shrinkage occurs only from the sides as illustrated in Fig. 1 B. Cells within the slightly shaded area are partially uncoupled, not because of diluted heptanol but because of the time for these cells to recover from the effects of the uncoupler. Myocytes on the boundary between the two regions experienced the concurrent changes in coupling and automaticity as cells recovered from the uncoupler and cAMP-mediated effects of isoproterenol were taking place. The washout process lasted 2.5 min, after which the area where the waves did not propagate disappeared.

Monitoring network behavior

Cells plated on laminin-covered coverslips were loaded with 5 μM Fluo-4AM for 1 h. Each spontaneous or paced action potential was associated with a calcium transient. Fluo-4 was excited at 488 nm, and the fluorescence was acquired at wavelengths of >515 nm. Experiments were conducted using a BioRad (Hercules, CA) MRC-1024 confocal imaging system with a low-power magnification objective (Olympus PlanApo 4×/0.16 NA). Conclusions are based on 22 experiments using five different cell preparations. The number of recorded events for a specific scenario is mentioned in parentheses within the corresponding sentence. Notably, the recorded cases are only a subset of the visually observed scenarios, i.e., the described sequence of events was observed in more experiments than it was recorded.

Numerical model

We used a generic Beeler-Reuter model of a cardiac myocyte (18), which contains an explicit, albeit simplified, description of individual ionic currents.
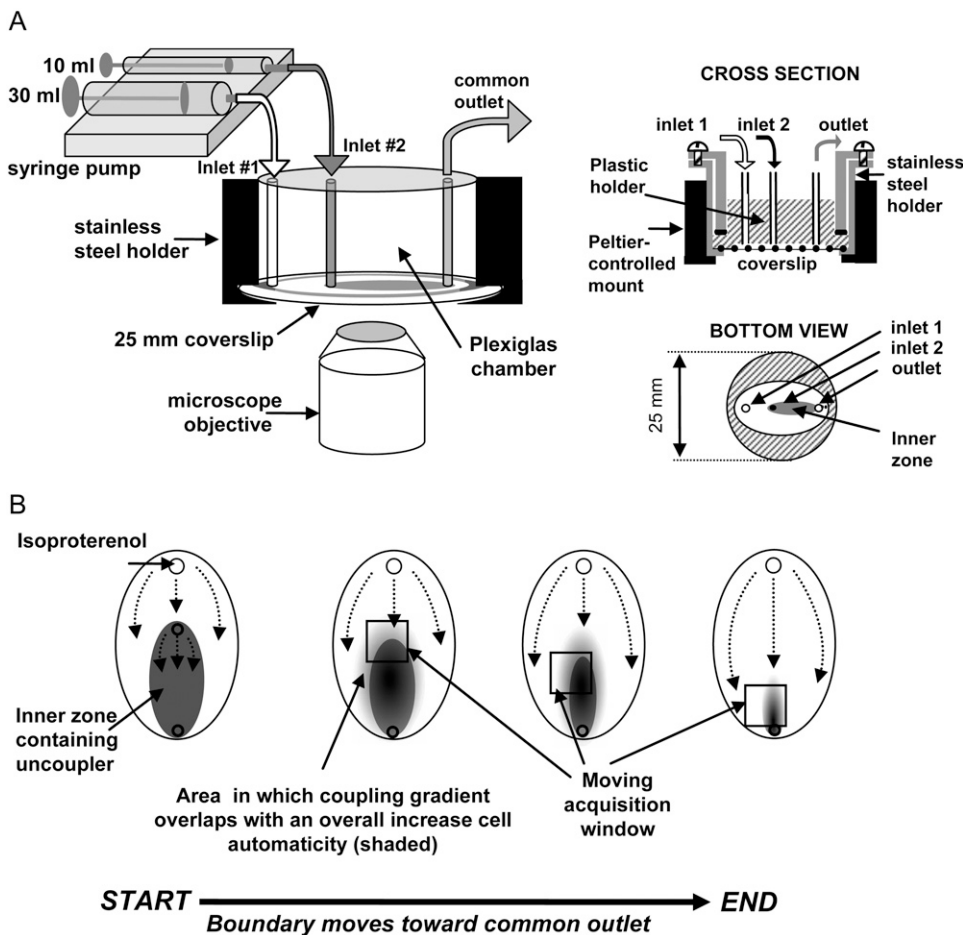

FIGURE 1 Experimental setup. (A) Schematics showing experimental setup, which includes multisyringe pump, custom-made perfusion chamber, and confocal imaging system in an inverted microscope configuration. (B) Cartoon illustrating experimental protocol, which included the washout of heptanol (gray) by the isoproterenol-containing solution (white). Lighter shades of gray indicate the areas with a sharp coupling gradient.

This model has proved to be an adequate tool to closely describe the events seen in our experimental preparations (17). The advantage of the model is that it is computationally simple, allowing us to simulate hundreds of thousands of cells with relative ease. It also offers a convenient way to modulate cell automaticity (details below).

The state of a cell is described by a membrane potential V satisfying

$$\partial_t V = -(I_{Na} + I_s + I_{K1} + I_{x1})/C + \text{coupling term},$$

where C is the capacitance per area of membrane, I_{Na} is the fast depolarizing sodium current, I_s is the slow depolarizing current, carried mostly by calcium, and I_{K1} and I_{x1} are two repolarizing potassium currents. These currents depend on membrane potential, cytosolic calcium concentration, and six gating variables. The currents were modified from the original Beeler-Reuter model: the gated ("time-dependent") component of I_{Na} was 60% of its standard value, I_s was 50% of its standard value (19), and I_{K1} was modified in a complex time- and space-dependent way as explained within the text. The voltage-dependent functions were tabulated for V in the range from -100 mV to 80 mV with a step 0.1 mV. The time stepping was done using an explicit Euler scheme for all variables with a time step of 0.1 ms. In simulations that employed a wider range of coupling values (see Fig. 5 for an example), the time step was decreased to 0.02 ms for stability purposes. The choices of voltage and time steps were dictated by consideration of accuracy and stability and were verified by varying the time step and ensuring that no essential changes in the features of interest occurred. The spatial step corresponded to typical intercellular distance and was not varied.

Spatial arrangement of cells in numerical model

We considered an idealized situation, where cells are located on a square lattice, so the variables are labeled by two integers, i and j, which label the rows and columns of the lattice respectively (Fig. 2, *step 1*). Cells are coupled to their nearest neighbors with

$$\text{coupling term}(i;j) = D/l^2 \, (V_{i+1;j} + V_{i-1;j} + V_{i;j+1} + V_{i;j-1} - 4V_{i;j}), \tag{1}$$

where the effective diffusion coefficient D is proportional to the conductivity between cells, and l is the distance between cells. We stress that Eq. 1 is not thought of here as a spatial discretization of a Laplacian term as in a "reaction-diffusion" system but represents Ohm's and Kirchhoff's laws and the assumed rectangular geometry of the grid of individual cells. Currents through boundaries of the grid were assumed to be zero. The value of l is set at 30 μm to account for the mean spacing between the centers of two adjacent cells, an estimate from experimental preparations. Velocity of propagation in isotropic cardiomyocyte networks at room temperature is $\sim$10–15 cm/s, which corresponds to $D \approx 0.10$ cm^2/s (17,20).

The gradient of coupling strength was oriented vertically as shown in Fig. 2, *step 1*, with the y-axis running from the bottom to the top. The upper layers corresponded to a more coupled region (D_{max}), and the bottom ones to a fully uncoupled region (D_{min}). An exponential gradient between the two D values was then applied to the middle, or what we will call hereafter the "boundary layer."

Numerical means to increase cell automaticity

Our aim was to describe a heterogeneous network that becomes spontaneously active as excitatory effects of isoproterenol or barium are developed. Thus, to make cells spontaneously active, we altered the balance between inward and outward currents by inhibiting the inward potassium rectifier current, I_{K1}, an approach taken by us and others in the past (17,21,22). By

Step 1: Spatial gradient of coupling

Step 2: Spatial profile of automaticity, α

Step 3: Increase in mean automaticity $\langle\alpha\rangle$

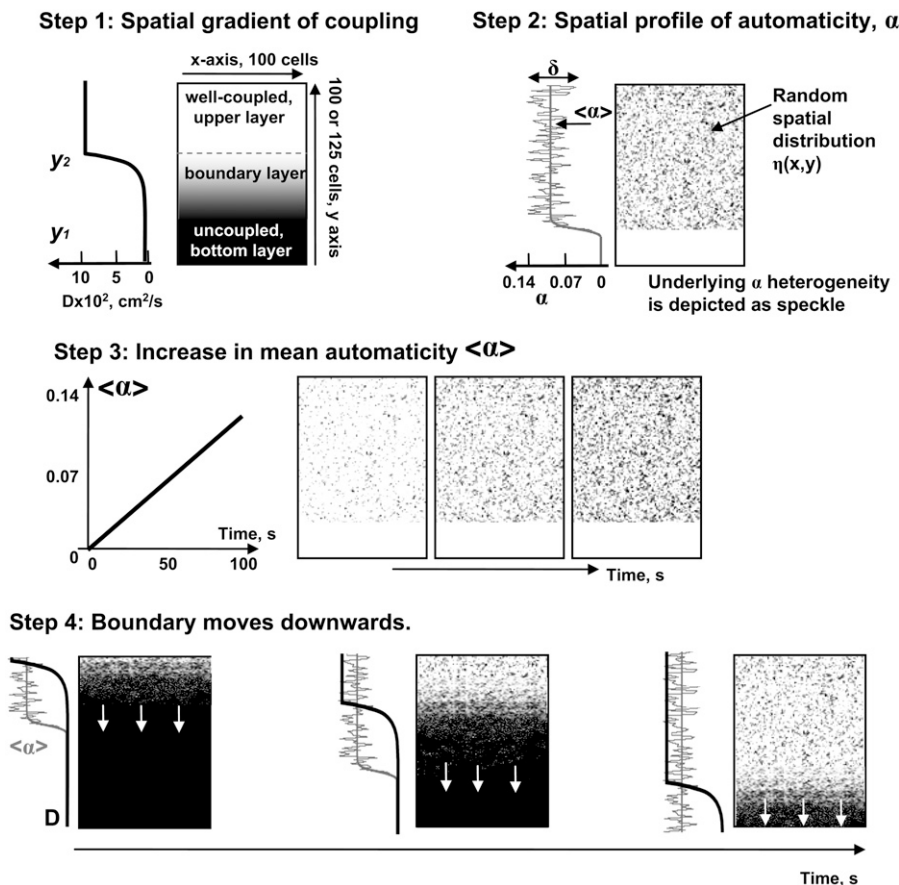**Step 4: Boundary moves downwards.**

FIGURE 2 Schematics showing the major steps involved in modeling the experimentally observed behavior. Details in Methods section.

setting the initial values of g_{K1} at 30%, we were able to mimic the smaller I_{K1} contribution reported for neonatal cardiomyocytes (23,24) as compared with the original Beeler and Reuter values for adult ventricular cells (18). Further decrease in the channel conductance g_{K1} led to a spontaneous firing of individual cells as it alters the balance between inward and outward currents (17). Changes to the conductance were implemented as $g_{K1} = 0.3 - \alpha(x,y,t)$, where the parameter α, hereafter referred to as "automaticity," was varied in space and time, with larger α values corresponding to a higher automaticity. For the bottom, fully uncoupled cells, α values were set to zero to reflect the fact that in our experiments neither isoproterenol nor barium was present in the heptanol solution (Fig. 2, *steps 2* and *3*). Notably, having or not having high automaticity in the inner zone would not make a difference in network behavior because cells there are fully uncoupled.

We want to stress that, in contrast to the spatial gradient of cell-to-cell coupling (as detailed below), α values exhibited step changes across few cells on the lower border. This was done to mimic our experimental setup, in which mixing or diffusion between the two flows creates a physical gradient of ~180 μm between the two solutions (14).

Numerical means to implement cell heterogeneity

The heterogeneity between individual cells was implemented by introducing two coefficients: $\eta(x,y)$ and δ. The first coefficient, $\eta(x,y)$, is a Gaussian-distributed uncorrelated random variable implemented using the Box-Muller 1958 transformation with a mean of zero and standard deviation of 1. It allowed us to randomly distribute cells with different properties in space. The second coefficient, δ, was introduced to describe the degree of dispersion from the mean value of automaticity $\langle\alpha\rangle$. For an individual cell with coordinates (x,y), automaticity was therefore described as $\alpha(x,y) = \langle\alpha\rangle(1 + \delta \ \eta(x,y))$. Temporal changes of automaticity were implemented by changing the $\langle\alpha\rangle$ value accordingly (summary in Table 1 and figure legends). These changes were implemented for the boundary and the upper layer. For the bottom, uncoupled cells, α values remained set to zero (Fig. 2, *step 3*). For the reader's convenience, we compiled all the values used in selected simulations and their corresponding movie files in Table 1.

Boundary movement in space

Our experimental settings mimicked a situation in which the ischemic (i.e., uncoupling) environment moves in space. In vivo, such a movement can be caused by reperfusion or by blood flow from a neighboring coronary bed as a result of local hyperemia. The boundary movement was implemented numerically as shown in Fig. 2, *step 4*. The mean automaticity values were set to a fixed value associated with multiple local waves of activity (see Table 1 for the parameters used in the specific simulations), and the coupling gradient was moved downward with a constant speed. The automaticity values moved together with the coupling gradient as shown in of Fig. 2, *step 4*. The speed of the downward movement was varied around the values seen in experiments.

RESULTS

Experimental studies

Observing the boundary on a cellular scale

Cells within the boundary layer between the two regions (denoted as a *gradient of gray color*, Fig. 1 *B*) experienced concurrent changes in coupling and automaticity. These changes occurred as a result of 1), recovery from heptanol; and 2), cyclic AMP-mediated effects of isoproterenol (16). These conditions led to a formation of multiple ectopic sources (Fig. 3), which appeared as multiple or individual waves next to the shrinking boundary (number of recorded cases: $n = 11$). Their wavefronts fused and spread outward, giving an impression of a single ectopic source (Fig. 3 *A*, *top row*). The position of the acquisition window relative to the uncoupled area is shown on the left (*black box*). It closely follows the spiral wave movement and therefore travels along the shrinking boundary. The speed at which the experimental boundary moved in space was not the same at all points along the boundary (because of the geometry of the inner area and the way it shrinks on washout); however, it was estimated to be in the range of 10–50 μm/s, or ~½–2 cells/s.

Spiral waves along the boundary

Ectopic sources gave rise to spiral waves, with durations ranging from 2 to 30 s (number of recorded cases: $n = 6$). Both clockwise and counterclockwise spiral waves were observed (Figs. 3 *A*, *middle row*, and 4 *A* and the corresponding movie

TABLE 1 Numerical parameters used in individual simulations, corresponding figures, and supplementary movies

Figure and corresponding movie file	Number of cells on x-axis	Number of cells on y-axis	Starting y coordinate that marks the lower part of the coupling gradient ($y_{1, \ t=0}$)	Starting y coordinate that marks the upper part of the coupling gradient ($y_{2, \ t=0}$)	Rate of boundary movement (cells/s)	Coefficient D of the uncoupled layer (cm²/s)	Coefficient D of the well-coupled layer (cm²/s)	Starting automaticity value $\langle\alpha\rangle_{t=0}$	Rate of automaticity increase $d\langle\alpha\rangle/dt$ (s⁻¹)	Dispersion coefficient, δ
5	100	125	25	75	0	10^{-5}	10^{-1}	0.08	10^{-3}	0.5
6 *A*	100	100	25	50	0	10^{-5}	10^{-3}	0	10^{-3}	0.25
6 *B*	100	100	25	50	0	10^{-5}	10^{-3}	0	10^{-3}	0.5
7 *A–C**	100	100	25	50	1/6	10^{-5}	10^{-3}	0.10	0	0.5
8 *D*†	100	100	65	95	1/10	5×10^{-5}	2×10^{-3}	0.12	0	0.5
9 *A*	100	100	70	95	3.5	10^{-5}	10^{-3}	0.12	0	0.5
9 *B*	100	100	70	95	7	10^{-5}	10^{-3}	0.12	0	0.5

*Fig. 7, *A–C*, shows three simulations with identical parameters but different spatial cell distributions. Fig. 8, *A* and *B*, uses the snapshots from the simulations shown in Fig. 7, *A* and *C*, respectively. Fig. 8 *C* is a magnified fragment of data shown in Fig. 8 *A*.
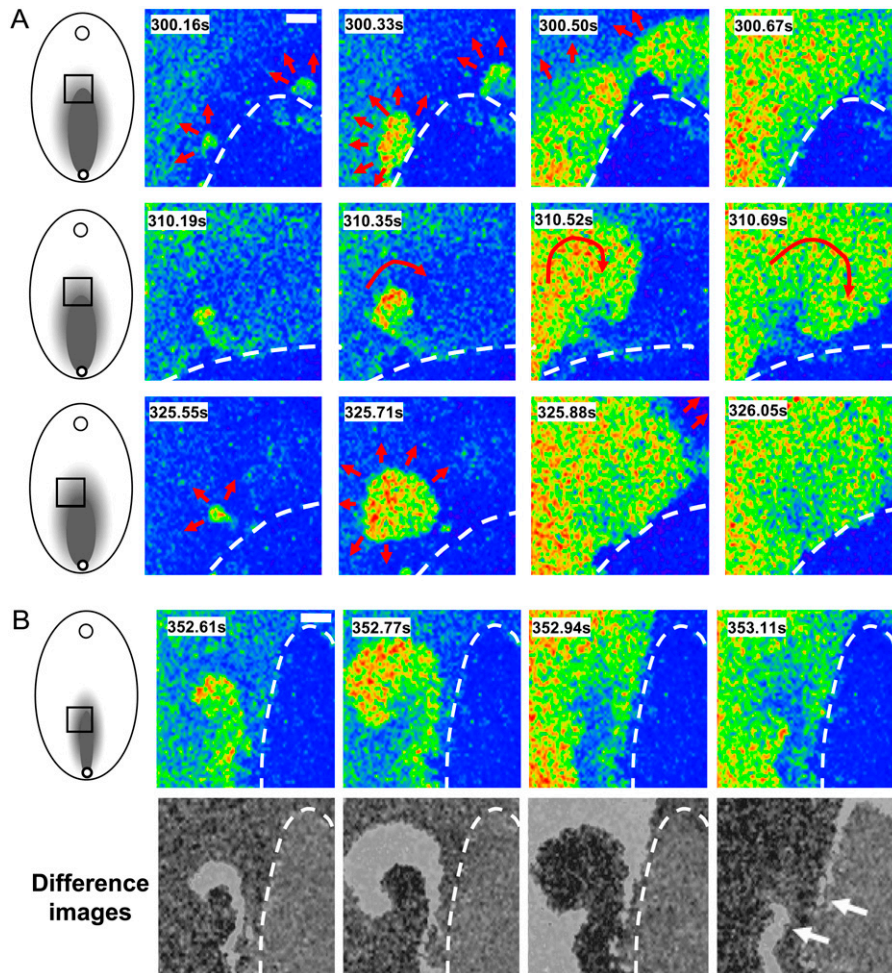†Fig. 8 *D* shows only a magnified fragment of the simulation data.

FIGURE 3 Experimental data illustrating continuous generation of target-like and spiral waves from the boundary layer. (A) Sequential images taken during one continuous recording. Each row illustrates the development of a particular wave pattern, including the appearance of multiple ectopic sources (*first row*), a clockwise rotating spiral (*second row*), and a single ectopic wave (*third row*). Arrows indicate direction of the wave spread. The dotted line shows the boundary of the uncoupled tissue. The acquisition window (*black box*) was moved during the experiment alongside the boundary to center each event. Note: Because the washout process was much longer (>2 min) than it took for an ectopic wave to spread through the entire field of view (<1 s), the boundary may appear static in these frames. The movement of the boundary can be clearly seen in the supplementary movie file. Scale bar is 0.5 mm. (B) Shape flattening of the spiral near the boundary. This occurs a a result of progressive wavelength shortening as conduction velocity sharply dropped near the uncoupled zone. This also created a ''shedding'' effect, when wavefronts from two or three previous spiral rotations are seen within the thin layer of cells near the uncoupled area (*arrows*). (*Top row*) Four sequential frames. (*Bottom row*) Difference frames (pixel value in the frame above minus the pixel value in the preceding frame), showing spread of activation. The full sequence of events can be seen in the corresponding movie file.

files). Once a spiral fully developed, it swept the entire cell network except the inner area blocked by the uncoupler. This suppressed individual ectopic sources, but they reappeared immediately after the spiral wave died off (number of recorded cases: $n = 5$). Another common feature observed in all cases was a flattening of the spiral shape. This effect results from a steep gradient of coupling and the corresponding gradient of conduction velocity: faster in the outside area, slower within the boundary. This sharp coupling gradient was also responsible for a wave ''shedding'' effect: near the boundary the wavelength becomes so short that wavefronts from two or more previous turns of a spiral were seen simultaneously next to each other (Fig. 3 B and the corresponding movie file). The white arrows point to the wavefronts from two sequential turns of the same spiral.

Trajectory of the spiral tip: sequential pinning

The majority of spirals born within the boundary layer represented transient events lasting two to five rotations. If a spiral persisted longer than a few seconds, it tended to travel along the interface between coupled and uncoupled cells (number of recorded cases: $n = 6$). As it did, the motion of the

spiral tip was noticeably nonstationary, with segments of pinned behavior alternating with periods of shifts along the boundary (Fig. 4 A and the corresponding movie file). With the orientation of the coupling gradient employed here, counterclockwise-rotating spirals tended to drift rightward, and the clockwise-rotating spirals drifted leftward. This is shown in Fig. 4 A via tip trajectories and can be observed during the first 6 s of the movie corresponding to Fig. 3 (leftward drift of a clockwise spiral in the first 6 s of the movie; rightward drift of a counterclockwise spiral 18–21s). In several cases ($n = 4$), spirals appeared to be anchored to the areas that, moments later, emitted circular ectopic waves (Figs. 3 A and 4 B). This suggests pinning of the spiral waves to the areas of altered automaticity, which agrees with our numerical studies discussed below.

Alternative treatments and control experiments

We tested an alternative approach to elevate cell automaticity. Specifically, in the above experiments, we replaced isoproterenol with barium chloride. Barium has been used as a tool to elevate cell automaticity by us and others (17,25). It does so by its direct inhibitory effect on the inward potassium rectifier
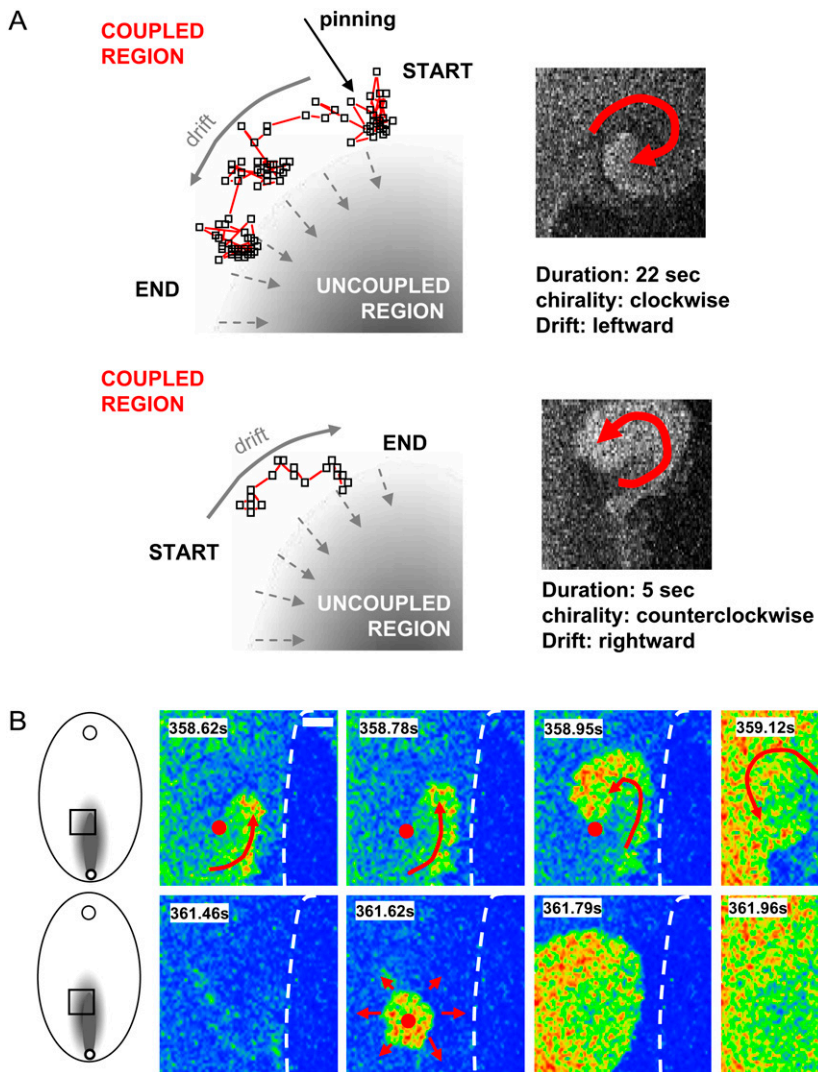
FIGURE 4 Drift and pinning of spiral waves in experimental settings. (*A*) The top panel illustrates the trajectory of a clockwise spiral reconstructed from sequential confocal frames. Each dot indicates coordinates of the spiral tip within an individual frame. The spiral lasted 22 s and drifted leftward. It was pinned in three spots. An example of a counterclockwise spiral is shown below. It lasted for a shorter period (5 s) and exhibited rightward drift. The full sequence of the events can be seen in the corresponding movie file. (*B*) Illustration of an attachment of the spiral to an area of elevated automaticity. (*Top row*) The last rotation of a spiral; tip position is marked by a red dot. (*Second row*) Target-like ectopic source appeared from the same spot immediately after spiral self-terminated.

current. Similar to the isoproterenol experiments described above, barium led to multiple localized rotating waves and ectopic sources on the boundary of the heptanol-containing area.

Control experiments were conducted using one treatment agent. Specifically, when isoproterenol was omitted from the perfusate, no ectopic activity was observed, and the heptanol-containing area shrank without apparent impact on the rest of the cell layer ($n = 8$). The effect of isoproterenol application without heptanol was associated with an increase in a monolayer's endogenous spontaneous firing rate ($n = 4$). The result was a single uniform wave rapidly passing through the entire coverslip (16). Barium application had a similar effect and was quantified by us previously (17). All in all, when applied by themselves, heptanol, isoproterenol, or barium did not produce patterns associated with local waves.

We note that macroscopic spiral waves can readily be induced in cardiomyocyte monolayers by either rapid pacing or cross-field or premature stimulation (26–28). We stress that the spiral activity reported here was not induced by external electrodes. The small rotating waves occurred spontaneously as a result of rapidly changing conditions on the boundary. Our next step was to explore these patterns numerically, as reported below.

Numerical studies

Behavior of the boundary layer

We started by creating a steep gradient in coupling (Fig. 2, *step 1*), represented by the coefficient D, stretching from what is considered to be normal D values (10^{-1} cm^2/s), to a fully uncoupled cell network ($D = 10^{-5}$ cm^2/s). Notably, the fourth-order magnitude change in D values was not an arbitrary choice but was dictated by experimentally observed propagation velocities. The latter differed by two orders of magnitude, from 12 cm/s in fully coupled cultures (17) to ~0.1 cm/s near the uncoupled area (Fig. 3 *B*: the scale bar is 0.5 mm, and the time stamp is on the top of the figures). The corresponding estimates of the gap junction conductivities

range between 300 and 0.03 nS, which matches experimental and numerical data by others (see Kleber and Rudy (29), Figs. 16 and 18 D). One should keep in mind that propagation at higher automaticity is akin to phase waves and requires much smaller conductivity than normal excitation waves, and our simulations as well as experiments spanned parametric areas where the propagation in fact did not happen.

Mean cell automaticity, represented by the value $\langle\alpha\rangle$, was set to increase within the boundary and the upper regions at a steady rate of $d\langle\alpha\rangle/dt = 0.001$ s^{-1} (Fig. 2, steps 2 and 3). The choice of $\langle\alpha\rangle$ values was not arbitrary but ranged from values at which the network was quiescent to values at which local waves appeared (17). Importantly, this increase in automaticity occurred nonuniformly, depending on individual cells' α values, with dispersion coefficient $\delta = 0.5$. Graphically, mean automaticity $\langle\alpha\rangle$ is shown as a bold gray line on the left of Fig. 2, step 2, and a thin gray line shows the distribution of individual α values for a column of cells with a fixed x coordinate.

Let us consider an example of one of these studies (Fig. 5). The specific parameters for each figure can be found in Table 1. The $\langle\alpha\rangle$ starts at 0.08 and increases with a rate of 0.001 s^{-1}. For the first 25 s no activity is observed in any of the zones (Fig. 5 A, first panel). At about $t = 27$ s ($\langle\alpha\rangle = 0.107$), several small ectopic sources start to appear at the cell layer with $D \approx 10^{-3}$ cm^2/s (Fig. 5 A, second panel). Waves generated by these ectopic sources do not spread to the upper layers because the strength of the excitatory currents is not sufficient to overcome the source/load mismatch caused by the coupling gradient. Waves also do not spread downward because

cells below were uncoupled. As mean automaticity $\langle\alpha\rangle$ increases, so does the area to which the local waves spread. They then start to interact with each other, forming spirals and other dynamic patterns (Fig. 5 and Supplementary Material, Movies). The local waves remain contained within the boundary layer until $\langle\alpha\rangle$ reaches the level of 0.117. After that waves start to exit the boundary and spread into the upper layers. The changing pattern of spirals and ectopic sources continues to exist within the boundary layer, but these sources were interacting with the waves returning from the upper zone. The quenching effect of these returning waves, amplified by a strong coupling in the upper layers, can be seen in the Fig. 5 movie. Notably, if one observes the events from the top layer, the overall activity of the boundary would appear as individual, somewhat irregular, ectopic beats exiting at random places.

The readers are asked to view the supplementary movies because they are an essential part of this report. Indeed, it is not trivial to reflect the observed dynamic events using a few sample frames such as those shown in Fig. 5 A. The time traces from two individual cells (one within the boundary and the other from the well-coupled upper layer) confirm that while the amplitude of averaged signals from the boundary is decreased due to a smaller amount of activated cells (Fig. 5 B), the amplitudes of action potentials from individual cells remain the same (Fig. 5 C). Change in cell membrane potential or intracellular calcium (Fig. 5 C) confirm that the records of calcium transients essentially reproduce the transmembrane potential recordings.

We have run several simulations using different spatial distributions of cells with all other parameters being identi-
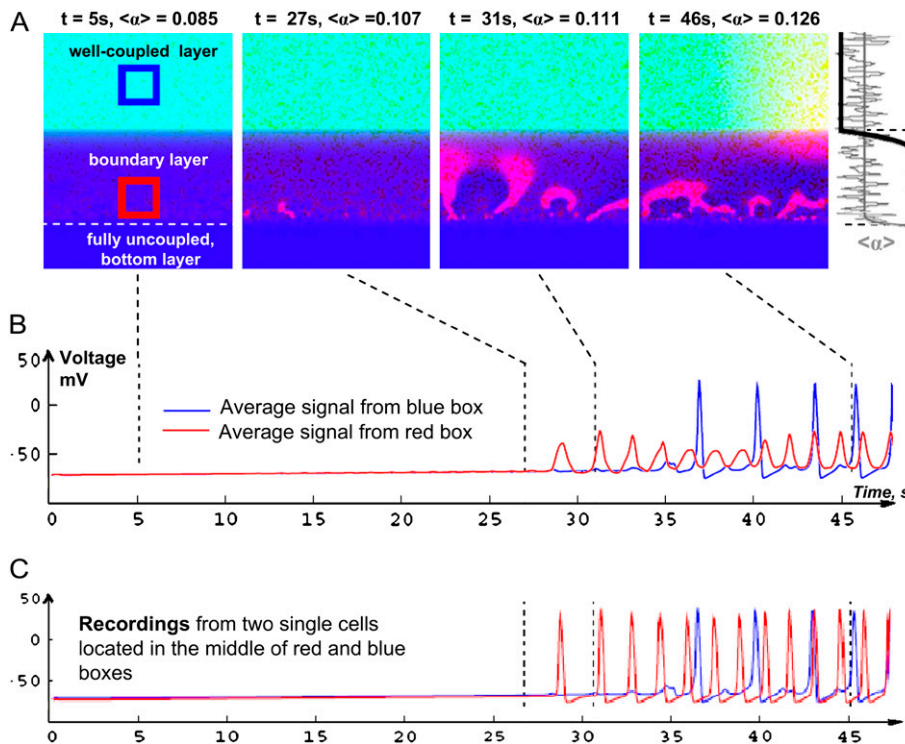

FIGURE 5 Numerical studies. Local waves forming within the boundary on implementation of the first three steps shown in Fig. 2. (A) Selected activation patterns from a simulation with growing $\langle\alpha\rangle$. Before $\langle\alpha\rangle$ reaches a certain value, no activity is present. Then multiple spontaneous ectopic sources ($t = 26$–29 s) and local waves ($t = 29$–36 s) start to appear within the boundary layer, and at about $t = 37$ s, this activity starts penetrating into the well-coupled layer. Full sequence of the events can be seen in the corresponding movie file. (B) The average activity from the areas A and B (voltage recordings). The dotted lines point to the corresponding snapshots in panel A. (C) A comparison between single-cell recordings from areas A and B.

cal. For each case, when $\langle\alpha\rangle$ values were substantially below critical, the local waves remained locked within layers of intermediate coupling because of the source/load mismatch. When $\langle\alpha\rangle$ values exceeded $\langle\alpha\rangle_{\mathrm{crit}}$, the waves started to propagate into the upper layers. Each case of spatial distribution $\eta(x,y)$ gave somewhat different scenarios of the generation of local waves and their escape.

The boundary layer shown in Fig. 5 has a very steep coupling gradient (D values ranging from 10^{-5} to 10^{-1} cm^2/s), which occurs over a narrow, 50-cell-wide layer of cells. Therefore, fusion and escape of local waves lead to an immediate activation of the entire upper layer (seen as a single yellow flash, Fig. 5 A). This is because the upper layer is fully coupled, and conduction velocity there is high as compared with the physical size of the medium represented by the box. To obtain more information about what affects the generation and escape of local waves, we ''zoomed in'' our simulations to the range of D values occurring just below the interface between the boundary layer and a well-coupled state. Therefore, in the next set of studies (Figs. 6–9), we considered events within a less steep coupling gradient (from 10^{-5} to 10^{-3} cm^2/s) with the upper layer corresponding to more weakly coupled network ($D = 10^{-3}$ cm^2/s). A much smaller wavelength (defined as the product of action potential duration and conduction velocity) allows clear visualization of the drift and escape of the tips of individual spiral waves into the upper layer.

Impact of cell heterogeneity

Our previous studies have suggested that individual cell heterogeneity is required to generate local waves (17). Specifically, if all members of the cell network were identical (in other words, dispersion coefficient, δ, was set to zero), the network would be either quiescent or all cells would fire simultaneously. Thus, we studied how the degree of automaticity heterogeneity affects the generation of local waves. As detailed in the Methods section, heterogeneity of automaticity

is determined by the two coefficients δ and $\eta(x,y)$. So, first we varied the dispersion coefficient, δ, while keeping spatial distribution $\eta(x,y)$ the same. In other words, the location of a cell with the highest α was the same, and thereby, the initial ectopic source was in the same place (Fig. 6 and the corresponding movie file). The overall result was that when the degree of dispersion was low, the ectopic activity started later and in fewer places.

When δ was kept the same but the spatial distribution of cells, $\eta(x,y)$, was varied, the location of individual ectopic sources was altered. The overall result, however, remained essentially the same; i.e., the effect of the specific location of individual cells within a static boundary was minor (data not shown). The spatial distribution of cells played a larger role when the boundary became dynamic, i.e., when it started to move in space as detailed immediately below.

Moving boundary

Our next steps were to fix the mean automaticity $\langle\alpha\rangle$ at a value associated with ectopic activity and to investigate the effect of boundary movement (Fig. 2, *step 4*). With a static spatial distribution, an ectopic source with the shortest period became dominant, creating a steady-state pattern of events. In contrast, when the boundary was moved, the dominant role passed from one ectopic source to another, such that the system was constantly in a transient state. This increased the possibility of wavebreaks being formed and escaping into the better-coupled layer (Fig. 7).

Fig. 7 also illustrates the role of the spatial distribution of cells, $\eta(x,y)$. It shows frames from a protocol implemented for three different cell networks with all parameters identical but with different spatial distributions. One can see that the escaping wavebreaks are formed at different locations and instants of time, leading to a different scenario in each case.

When the boundary moves, the spiral tip might exhibit a pin-unpin type of drift. This is a result of a combination of the
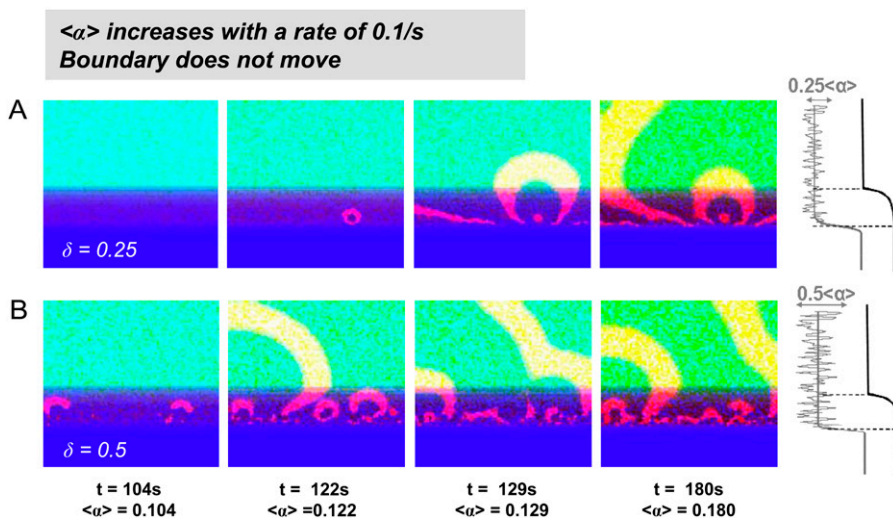

FIGURE 6 The impact of automaticity dispersion. The mean automaticity $\langle\alpha\rangle$ steadily grows with a rate of 0.001 s^{-1}. The cartoon on the right side shows the automaticity dispersion along an arbitrary vertical line. (*Top row*) Dispersion coefficient is $\delta = 0.25$. The number of ectopic sources is small, and the activity appears later ($t \approx 122$ s). (*Bottom row*) Dispersion coefficient is $\delta = 0.5$. More ectopic sources are present, and the activity appears sooner ($t \approx 104$ s).
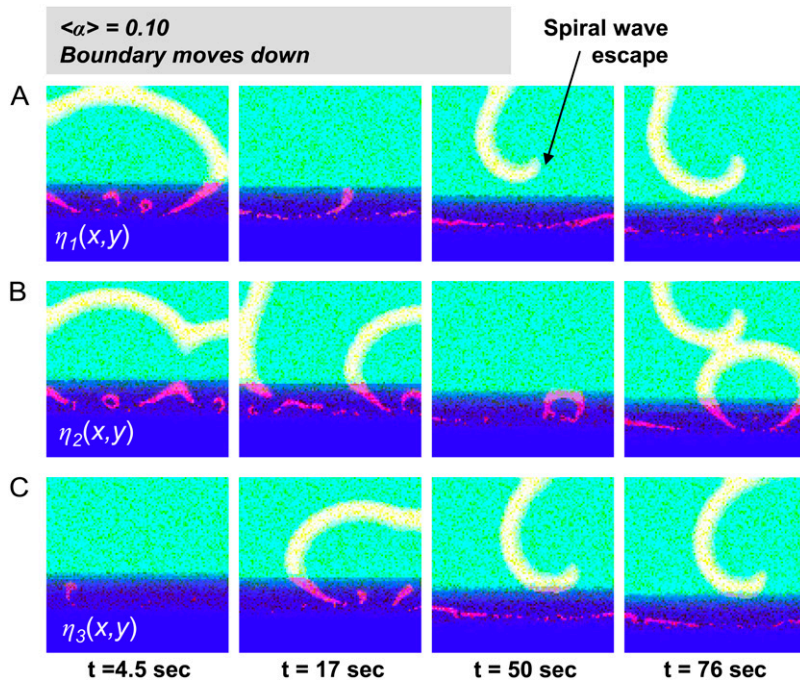
FIGURE 7 Impact of spatial cell distribution. The mean automaticity $\langle \alpha \rangle$ is fixed at 0.10, and the boundary moves downward with the speed of 1/6 cells/s. Cases shown in A, B and C differ only in the cells' spatial distribution $\eta(x,y)$.

microscopic cell heterogeneity and the macroscopic gradient of coupling. The direction of the drift observed numerically was in agreement with our experimental data (Fig. 4 A). The rightward drift of a counterclockwise spiral can be seen in Fig. 8 A and its corresponding movie file. Another example can be seen in the movie file corresponding to Fig. 9 A (*right panel*). An example of leftward drift of a clockwise spiral is shown in Fig. 8 B.

Drift of spiral waves caused by spatial gradients is well known in the theory of excitable media. The dominant mechanism of drift in our case was described by Pertsov and Ermakova (30): the tip turns faster in the upper, more-coupled
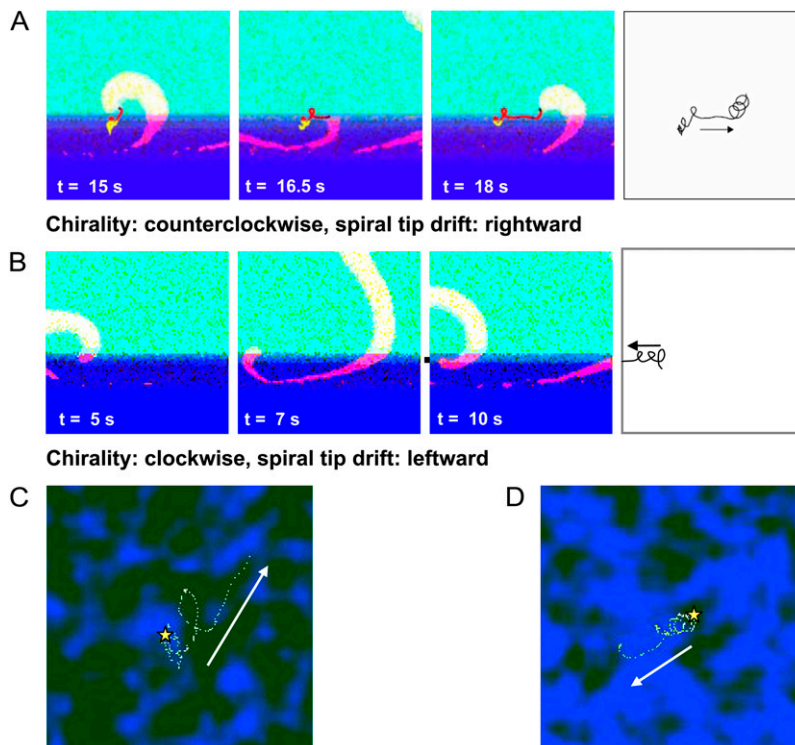

FIGURE 8 Pin-unpin drift and the coupling gradient. The mean automaticity $\langle \alpha \rangle$ is fixed at 0.10, and the boundary moves downward with the speed of 1/6 cells/s. Selected frames from two different simulations illustrate the rightward (A) and leftward (B) drift alongside the boundary interface. The tip trajectory reflects erratic pin-unpin behavior. Sequence shown in A can be seen in the corresponding movie file. The two bottom panels show magnified pieces of tip trajectories on the background of the $\eta(x,y)$ distribution in two different stimulations. The $\eta(x,y)$ distributions have been smoothed by a 9×9 cell sliding window, and color-coding (*blue component representing* g_{K1}) adjusted to embellish the pinning clusters (*marked by stars*). In C (fragment of the same simulation as in A), the spiral before unpinning was attached to a bright-blue (high g_{K1}, suppressed automaticity) cluster. In D (a different simulation), the spiral before unpinning was attached to a dark-green (low g_{K1}, elevated automaticity) cluster.
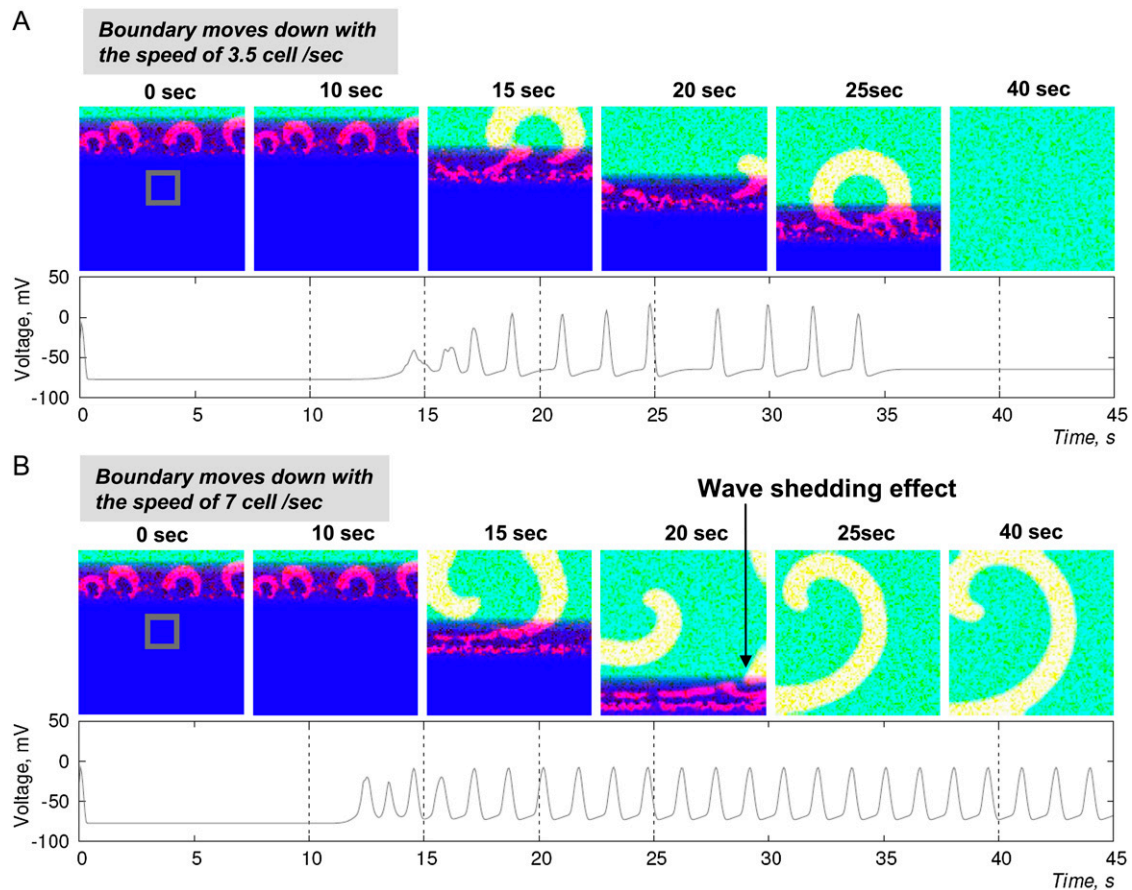
FIGURE 9   The speed of coupling gradient movement determines the probability of wavebreak escape. The spatial distribution $\eta(x,y)$ was identical for the cases shown in A and B. The mean automaticity $\langle\alpha\rangle$ is fixed at 0.12. The only difference is the speed of the downward movement of the boundary. (A) Boundary moves slowly (3.5 cells/s), and wavebreaks (i.e., tip of the spiral) do not escape. Therefore, when boundary passes, no waves remain. (B) Boundary moves faster (7 cells/s). The wavebreak escapes into the better-coupled layers. After the boundary passes, the spiral wave continues to rotate. The full sequence of events shown in A and B can be seen in the corresponding movie file.

layer than in the lower, less-coupled layer. Therefore, the upper segments of the tip trajectory are shorter than the lower segments and the spiral drifts. However, the above-mentioned theoretical works were for systems with macroscopic gradients. In our case, we have microscopic heterogeneity, expressed via dispersion in automaticity values of individual cells. The effect of this heterogeneity is a pin-unpin type of drift, which was also seen in experiments (Fig. 4 A).

Let's consider the simulation shown in Fig. 8 A in more detail. It is a numerical example of an "exaggerated" Pertsov-Ermakova drift mechanism. Visual analysis of this episode, as well as others, illustrates the general tendency for the tip to stick to clusters of cells with different properties, such as suppressed (Fig. 8 C) or elevated (Fig. 8 D) automaticity. Notably, in the experiments, many, but not all, sites where spirals were pinned later became foci, i.e., they have underlying high-automaticity clusters (Fig. 4 B). Of course, if it had been a low-automaticity cluster, then cells would not have spontaneously activated, and such a cluster would be unnoticed (note: a cluster consisting of few cells would not impact macroscopic conduction to a measurable extent). As the

gradient approaches, the spiral unpins and drifts. With the orientation of the tip as at $t = 16.5$ s (Fig. 8 A, *middle frame*) and with the coupling above much higher than that below, movement of the wave tip upward is impeded by the source/load mismatch. The latter effectively reduces the automaticity at the tip and prevents it from turning. Hence, we observe an almost straight segment of the tip trajectory as the tip "glides" along the coupling interface. Such straight motion continues until the tip reaches a more excitable locus and/or an area with a smaller coupling gradient, where it stops.

When the boundary moved at a higher speed, the probability of a spiral tip escaping into a more coupled area increased. As an example, Fig. 9 shows parallel frames from the two simulations with all parameters identical, including spatial distribution $\eta(x,y)$ and dispersion coefficient, δ. The only difference was the speed at which the boundary layer was moving. The fast-moving boundary (7 cells/s) caused the tip of a spiral wave to escape, whereas the slower one (3.5 cells/s) did not. Similar results were observed when we expanded our studies to three dimensions (data not shown), a subject to be discussed in a separate publication.

DISCUSSION

Our data represent one of the first attempts to mimic complex boundary behavior in a heterogeneous cell network. Certain assumptions and simplifications had to be made to accomplish this task. These included the following:

Experimental model

Our study dealt with neonatal cardiomyocyte preparations that beat spontaneously, albeit at slow rates (0.2–0.5 Hz at room temperature). Therefore, our interventions with either isoproterenol or barium simply elevated the endogenous automaticity of these cells. How can these events be related to myocardial tissue composed of quiescent adult ventricular myocytes?

The answer is our growing understanding that "true automaticity" and "triggered activity" are two sides of the same coin. Originally, the first meant a spontaneous, stand-alone pacemaker-like behavior, whereas the second required a preceding action potential to occur and was facilitated by calcium overload (31). However, the distinction between these two terms has become less and less clear, as "spontaneous" triggered activity caused by leakiness of SR, calcium overload, elevated $I_{ns,Ca}$ and $I_{Cl(Na)}$, or upregulation of the Na/Ca exchanger became apparent (32). Moreover, recent evidence suggests the main mechanism behind triggered activity in ventricular cells (calcium leak from the sarcoplasmic reticulum, followed by Ca/Na exchanger current) is also a major cause of automaticity in classical pacemakers, i.e., sinoatrial cells (33,34). Therefore, instead of opposing the concepts of automaticity and triggered activity, we refer to spontaneously active myocytes, regardless of their underlying mechanism, as "ectopics." The above arguments support the use of neonatal cardiomyocyte cultures as a model system to analyze behavior of ventricular tissue in which myocytes are made spontaneously active by pathological conditions.

Wave monitoring

Our experimental data were based on monitoring of calcium transients using the calcium-sensitive fluorescent indicator Fluo-4. This approach is widely used to follow propagating waves in cardiac muscle (26,35,36). Under control conditions, Ca_{in} transients immediately follow electrical activity, and wave propagation patterns are essentially identical (37,38). Notably, during the initial stages of ectopic wave generation, this sequence may be reversed; i.e., depolarization may follow the elevation of cytosolic calcium (39). Thus, in addition to its high fidelity, monitoring of Ca_{in} instead of transmembrane voltage ensures that the earliest signs of ectopic activity are recorded. It is important to stress that intercellular waves observed in our studies represent spreading electrical activity and should not be confused with so-called intracellular calcium waves. Intracellular calcium waves are confined to individual myocytes and are much slower (0.1

mm/s) than the velocities of local waves observed in our preparations. The latter ranged from 10 to 15 cm/s in control conditions and to 0.5 cm/s in areas starting to recover from heptanol.

Experimental means to increase cell automaticity

In vivo, a multitude of factors, including extracellular potassium, pH, ATP, neuropeptides, and intra- and extracellular calcium can cause a myocyte to reach depolarization threshold and fire an action potential (31). The subject of our studies, however, is not an individual cell but a cell network. For the latter, the behavior is a result of mutual interaction as well as timing and location of the individual myocytes after they have passed their individual thresholds. Therefore, we simplified the multiple factors noted above into a single intervention that increased myocyte activity. The experimental data presented here correspond to experiments with the β-adrenergic agonist isoproterenol (16,40). An alternative way to increase myocyte automaticity is to use barium chloride, which inhibits inward potassium rectifier current (I_{K1}). The latter increases cardiomyocyte firing rate in a concentration-dependent manner (17). Our experiments with barium chloride produced phenomenologically similar results (data not shown).

Numerical means of increasing automaticity

Inhibition of I_{K1} is not exactly a physiological way to mimic triggered activity during either ischemia or reperfusion. We used this approach as a convenient and established numerical tool to make cells automatic using Beeler-Reuter numerics. Much more detailed numerical models are required to fully simulate the effect of catecholamines or calcium overload, which induces triggered activity within individual myocytes, because one needs to take into account effects of calcium release from intracellular stores as well as geometry/spatial arrangements of adjacent intercellular compartments. The effect achieved by I_{K1} inhibition is rather generic: it tilts the balance between inward and outward currents. The advantage of this particular model was the possibility of using the knowledge of the parameter space of the model, achieved in our previous work; there the model was carefully fitted to reproduce our experimental preparations (17). Further studies will be required to extend our conclusions derived from model systems to more relevant physiological scenarios. The semi-phenomenological description presented here simply suggests plausible scenarios and formulates interesting questions for subsequent more detailed studies.

CONCLUSIONS

With the assumptions and limitations noted above, we made the following conclusions from the bulk of the in vitro and numerical data. First, the data suggest that the combination of the two gradients (i.e., the spatial gradient in cell-to-cell
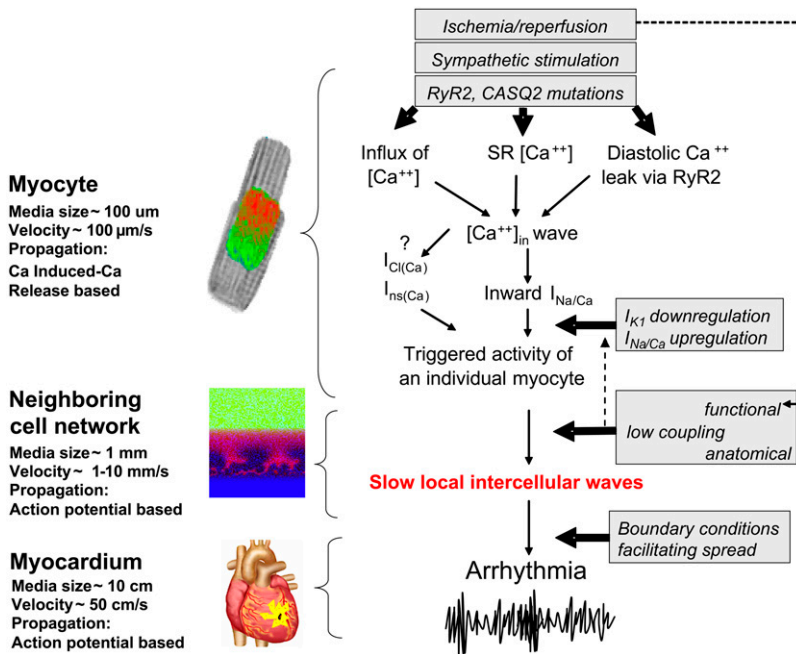
FIGURE 10 Flow diagram that illustrates the potential pathophysiological significance of local waves. The top part incorporates current beliefs (adapted from Rubart and Zipes (41)) of how a variety of triggers might lead to spontaneous cell firing. RyR2, ryanodine receptors; CASQ2, calsequestrin; $I_{Cl(Ca)}$, calcium-activated Cl current; $I_{ns(Ca)}$, nonspecific cation current. The local waves appear to be an essential intermediate step that facilitates the spread of the triggered activity from individual cells into well-coupled myocardial tissue.

coupling and the temporal gradient in cell automaticity) ensures that somewhere within the boundary there is a region where multiple ectopic sources are continuously being formed. They are highly localized focal points of activity, with activation spreading only to a few surrounding cells. The number of ectopic sources and the specific window of conditions when they occur are affected by the degree of network heterogeneity. Second, our data argue that if the ectopically active layer is sufficiently wide and/or the overall cell automaticity rises, ectopic sources develop into target-like waves. If a coupling gradient and automaticity levels remain spatiotemporally fixed, the pattern of target-like sources persists, and no spiral activity is observed. However, when cell automaticity rises and/or the boundary moves in space, the propagation patterns become nonstationary. This leads to multiple wavebreaks and spiral activity. Spiral waves typically demonstrate start-stop drifting behavior, as a result of competing forces between pinning force from local heterogeneity and gradient-induced directional drift. The likelihood of spiral escape into better-coupled tissue depends on the speed at which the boundary moves in space.

We are a long way from concluding that the patterns observed here can be found within inner layers of diseased myocardium and/or are the precursors of ectopic beats in vivo of ectopic beats. Indeed, it is unlikely that in vivo the formation and escape of local waves occur in the exact way these are portrayed in our figures. However, one has to consider that a wide window of conditions does occur when blood flows into the complex fractal surface of a previously occluded coronary artery bed. On such a moving boundary, one can imagine a sharp coupling gradient together with rapidly recovering cell excitability as interstitial pH, potassium, and oxygen levels are being restored while levels of interstitial

norepinephrine are elevated. Therefore, it is hard to deny the probability that, within small regions of moving boundary, there will be a range of coupling and automaticity values that could breed local waves. Fig. 10 places them in a larger pathophysiological context. The upper part explains how an individual, quiescent myocyte turns into a cell that spontaneously fires an action potential (41). How likely is it for spontaneously triggered activity to occur synchronously in a large number of cells? This is an important question because if activation does not involve a critical number of cells, a wave will not form. Therefore, an additional step is required between the triggered activity of individual cells and the arrhythmia on the level of the whole heart. The slow, local intercellular waves, similar to the regimes considered in this article, appear to be the required step for the ectopic beats to be formed. We feel that the characterization of these regimes is important and that an awareness of such activity can facilitate its future detection in vivo.

SUPPLEMENTARY MATERIAL

To view all of the supplemental files associated with this article, visit www.biophysj.org.

REFERENCES

1. Dhein, S. 2006. Cardiac ischemia and uncoupling: gap junctions in ischemia and infarction. *Adv. Cardiol.* 42:198–212.

2. Stevenson, W. G., J. N. Weiss, I. Wiener, and K. Nademanee. 1989. Slow conduction in the infarct scar: relevance to the occurrence, detection, and ablation of ventricular reentry circuits resulting from myocardial infarction. *Am. Heart J.* 117:452–467.

3. Peters, N. S. 1996. New insights into myocardial arrhythmogenesis: distribution of gap-junctional coupling in normal, ischaemic and hypertrophied human hearts. *Clin. Sci. (Lond.).* 90:447–452.

4. Elizari, M. V., and P. A. Chiale. 1993. Cardiac arrhythmias in Chagas' heart disease. *J. Cardiovasc. Electrophysiol.* 4:596–608.

5. Kies, P., M. Bootsma, J. Bax, M. J. Schalij, and E. E. van der Wall. 2006. Arrhythmogenic right ventricular dysplasia/cardiomyopathy: screening, diagnosis, and treatment. *Heart Rhythm.* 3:225–234.

6. Peters, N. S., and A. L. Wit. 1998. Myocardial architecture and ventricular arrhythmogenesis. *Circulation.* 97:1746–1754.

7. Mills, W. R., N. Mal, M. J. Kiedrowski, R. Unger, F. Forudi, Z. B. Popovic, M. S. Penn, and K. R. Laurita. 2007. Stem cell therapy enhances electrical viability in myocardial infarction. *J. Mol. Cell. Cardiol.* 42:304–314.

8. White, R. L., J. E. Doeller, V. K. Verselis, and B. A. Wittenberg. 1990. Gap junctional conductance between pairs of ventricular myocytes is modulated synergistically by H^+ and Ca^{++}. *J. Gen. Physiol.* 95:1061–1075.

9. Yamada, K. A., J. McHowat, G. X. Yan, K. Donahue, J. Peirick, A. G. Kleber, and P. B. Corr. 1994. Cellular uncoupling induced by accumulation of long-chain acylcarnitine during ischemia. *Circ. Res.* 74:83–95.

10. Lameris, T. W., S. de Zeeuw, G. Alberts, F. Boomsma, D. J. Duncker, P. D. Verdouw, A. J. Veld, and A. H. van Den Meiracker. 2000. Time course and mechanism of myocardial catecholamine release during transient ischemia in vivo. *Circulation.* 101:2645–2650.

11. Warner, M. R., P. L. Wisler, T. D. Hodges, A. M. Watanabe, and D. P. Zipes. 1993. Mechanisms of denervation supersensitivity in regionally denervated canine hearts. *Am. J. Physiol.* 264:H815–H820.

12. Karmazyn, M., X. T. Gan, R. A. Humphreys, H. Yoshida, and K. Kusumoto. 1999. The myocardial Na(+)-H(+) exchange: structure, regulation, and its role in heart disease. *Circ. Res.* 85:777–786.

13. Zipes, D. P., and M. Rubart. 2006. Neural modulation of cardiac arrhythmias and sudden cardiac death. *Heart Rhythm.* 3:108–113.

14. Arutunyan, A., D. R. Webster, L. M. Swift, and N. Sarvazyan. 2001. Localized injury in cardiomyocyte network: a new experimental model of ischemia-reperfusion arrhythmias. *Am. J. Physiol. Heart Circ. Physiol.* 280:H1905–H1915.

15. Arutunyan, A., L. Swift, and N. Sarvazyan. 2004. Multiple injury approach and its use for toxicity studies. *Cardiovasc. Toxicol.* 4:1–10.

16. Arutunyan A, A Pumir, VI Krinsky, LM Swift, N Sarvazyan. 2003. Behavior of ectopic surface: effects of *β*-adrenergic stimulation and uncoupling. *Am. J. Physiol. Heart Circ. Physiol.* 285:H2531–H2542.

17. Pumir, A., A. Arutunyan, V. Krinsky, and N. Sarvazyan. 2005. Genesis of ectopic waves: role of coupling, automaticity, and heterogeneity. *Biophys. J.* 89:2332–2349.

18. Beeler, G. W., and H. Reuter. 1977. Reconstruction of the action potential of ventricular myocardial fibres. *J. Physiol.* 268:177–210.

19. Pumir, A., and V. Krinsky. 1999. Unpinning of a rotating wave in cardiac muscle by an electric field. *J. Theor. Biol.* 199:311–319.

20. Keener, J., and J. Sneyd. 1998. *Mathematical Physiology.* Springer Verlag, Berlin.

21. Silva, J., and Y. Rudy. 2003. Mechanism of pacemaking in I(K1)-downregulated myocytes. *Circ. Res.* 92:261–263.

22. Dhamoon, A. S., and J. Jalife. 2005. The inward rectifier current (IK1) controls cardiac excitability and is involved in arrhythmogenesis. *Heart Rhythm.* 2:316–324.

23. Masuda, H., and N. Sperelakis. 1993. Inwardly rectifying potassium current in rat fetal and neonatal ventricular cardiomyocytes. *Am. J. Physiol.* 265:H1107–H1111.

24. Wahler, G. M. 1992. Developmental increases in the inwardly rectifying potassium current of rat ventricular myocytes. *Am. J. Physiol.* 262:C1266–C1272.

25. Shen, J. B., and M. Vassalle. 1996. Barium-induced diastolic depolarization and controlling mechanisms in guinea pig ventricular muscle. *J. Cardiovasc. Pharmacol.* 28:385–396.

26. Agladze K, MW Kay, V Krinsky, N Sarvazyan. 2007. Interaction between spiral and paced waves in cardiac tissue. *Am. J. Physiol. Heart Circ. Physiol.* 293:H503–H513.

27. Entcheva, E., S. N. Lu, R. H. Troppman, V. Sharma, and L. Tung. 2000. Contact fluorescence imaging of reentry in monolayers of cultured neonatal rat ventricular myocytes. *J. Cardiovasc. Electrophysiol.* 11:665–676.

28. Iravanian, S., Y. Nabutovsky, C. R. Kong, S. Saha, N. Bursac, and L. Tung. 2003. Functional reentry in cultured monolayers of neonatal rat cardiac cells. *Am. J. Physiol. Heart Circ. Physiol.* 285:H449–H456.

29. Kleber, A. G., and Y. Rudy. 2004. Basic mechanisms of cardiac impulse propagation and associated arrhythmias. *Physiol. Rev.* 84:431–488.

30. Pertsov, A. M., and E. A. Ermakova. 1988. Mechanism of the drift of a spiral wave in an inhomogeneous medium. *Biofizika.* 33:338–342.

31. Carmeliet, E. 1999. Cardiac ionic currents and acute ischemia: from channels to arrhythmias. *Physiol. Rev.* 79:917–1017.

32. Ter Keurs, H. E., and P. A. Boyden. 2007. Calcium and arrhythmogenesis. *Physiol. Rev.* 87:457–506.

33. Bogdanov, K. Y., V. A. Maltsev, T. M. Vinogradova, A. E. Lyashkov, H. A. Spurgeon, M. D. Stern, and E. G. Lakatta. 2006. Membrane potential fluctuations resulting from submembrane Ca^{2+} releases in rabbit sinoatrial nodal cells impart an exponential phase to the late diastolic depolarization that controls their chronotropic state. *Circ. Res.* 99:979–987.

34. Bers, D. M. 2006. The beat goes on: diastolic noise that just won't quit. *Circ. Res.* 99:921–923.

35. Bub, G., L. Glass, N. G. Publicover, and A. Shrier. 1998. Bursting calcium rotors in cultured cardiac myocyte monolayers. *Proc. Natl. Acad. Sci. USA.* 95:10283–10287.

36. Entcheva, E., Y. Kostov, E. Tcherner, and L. Tung. 2004. Fluorescence imaging of electrical activity in cardiac cells using an all-solid-state system. *IEEE Trans. Biomed. Eng.* 51:333–341.

37. Entcheva, E., and H. Bien. 2006. Macroscopic optical mapping of excitation in cardiac cell networks with ultra-high spatiotemporal resolution. *Prog. Biophys. Mol. Biol.* 92:232–257.

38. Laurita, K. R., and A. Singal. 2001. Mapping action potentials and calcium transients simultaneously from the intact heart. *Am. J. Physiol. Heart Circ. Physiol.* 280:H2053–H2060.

39. Lakkireddy, V., G. Bub, P. Baweja, A. Syed, M. Boutjdir, and N. El-Sherif. 2006. The kinetics of spontaneous calcium oscillations and arrhythmogenesis in the in vivo heart during ischemia/reperfusion. *Heart Rhythm.* 3:58–66.

40. Schlotthauer, K., and D. M. Bers. 2000. Sarcoplasmic reticulum Ca^{2+} release causes myocyte depolarization. Underlying mechanism and threshold for triggered action potentials. *Circ. Res.* 87:774–780.

41. Rubart, M., and D. P. Zipes. 2005. Mechanisms of sudden cardiac death. *J. Clin. Invest.* 115:2305–2315.